

Topologically protected Q-switching for a pair of the Exceptional points in an optical microcavity laser

Kyu-Won Park,^{1,*} KyeongRo Kim,^{2,†} Jinuk Kim,³ Muhan Choi,⁴ and Kabgyun Jeong^{2,5,‡}

¹*Department of Mathematics and Research Institute for Basic Sciences, Kyung Hee University, Seoul, 02447, Korea*

²*Research Institute of Mathematics, Seoul National University, Seoul 08826, Korea*

³*Korea Research Institute of Standards and Science, Daejeon 34113, Korea*

⁴*Digital Technology Research Center, Kyungpook National University, Daegu 41566, Korea*

⁵*School of Computational Sciences, Korea Institute for Advanced Study, Seoul 02455, Korea*

(Dated: January 3, 2025)

The development of topologically protected systems is crucial for achieving robustness against noise, with significant applications in fields such as topological quantum matter and quantum computation. Exceptional points (EPs) in an optical microcavity laser, inherent to non-Hermitian systems, are pivotal in realizing these systems due to their nontrivial topological structures. Encircling EPs enables unique phenomena, including asymmetric mode switching and braid. Here, we demonstrate that topologically protected mode switching can be achieved in a two-level system without requiring non-adiabatic transitions and chiral behavior, leveraging braid isotopy. Moreover, a pair of EPs exhibiting super-radiance and sub-radiance enables both topologically protected mode switching and Q-switching. These results deepen our understanding of EP physics and present new opportunities for advanced applications in laser Q-switching.

PACS numbers: 42.60.Da, 42.50.-p, 42.50.Nn, 12.20.-m, 13.40.Hq

INTRODUCTION

In practical physical systems, robustness against noise and errors is essential for reliable implementation and application. Topologically protected systems inherently provide this robustness due to their resistance to external disturbances. These systems are widespread in topological quantum matter, such as topological insulators and superconductors, which exhibit immunity to disorder [1–3]. By exploiting these properties, topological quantum computation enables fault-tolerant information processing [4, 5]. Moreover, these systems have found significant applications in photonic meta-materials for robust light manipulation [6, 7] and in spintronics for efficient information processing [8, 9].

In this study, we propose that a pair of exceptional points (EPs) in non-Hermitian systems, characterized by their nontrivial topological structures, can serve as a novel platform for achieving both topologically protected mode switching and Q-switching. Real-world physical systems are typically non-Hermitian (open) due to their inability to be completely isolated from their environment [10]. These openness effects are manifested in the vicinity of a singular point known as the exceptional point (EP) in a parameter space, where at least two eigenvalues and their corresponding eigenstates coalesce simultaneously [11, 12].

Exceptional points have been studied both theoretically and experimentally in various physical systems, including carbon nanotubes [13], nano-optomechanical systems [14, 15], photonic crystals [16, 17], optical microcavities [18, 19], magnon-polariton systems [20, 21], and electrical circuit resonators [22]. EPs give rise to several in-

triguing phenomena associated with parity-time symmetry [23, 24], phase transitions [25, 26], chirality [27, 28], and Shannon entropy [29]. Furthermore, EPs have found applications in sensors [18, 30, 31], gyroscopes [32, 33], braid [34–36], and asymmetric mode switching [37–41].

In this work, we extend the conventional asymmetric mode switching mechanism to enable its application to Q-switching in laser physics. Conventional Q-switching techniques, whether active or passive, necessitate precise and complex control over the laser cavity's quality factor (Q) [42, 43]. Active Q-switching generally relies on electro-optic or acousto-optic modulators to rapidly alter the Q factor, thereby triggering pulse generation [44–46]. In contrast, passive methods employ saturable absorbers that adjust the Q factor once a certain threshold is surpassed [47–49]. While effective, these methods often require fine-tuned control and are susceptible to errors and performance degradation. Also, conventional mode switching typically involves chiral behavior and non-adiabatic processes during the adiabatic encircling of an EP [37–41]. This causes the loop on the Riemann surface to move off, resulting in a sudden state change despite the overall adiabatic process. Such characteristics impose significant limitations on achieving robust mode switching.

In contrast, by utilizing a pair of EPs exhibiting super-radiance and sub-radiance, we eliminate the need for non-adiabatic transitions and chiral behavior. Simply adiabatically encircling the EP independent of the specific loop configuration suffices to achieve both mode switching and Q-switching within a simple two-level system. This approach simplifies conventional methods and offers a topologically protected mechanism for Q-switching, in-

herently providing robustness against noise and system errors.

INTRODUCTION TO NON-HERMITIAN HAMILTONIAN

A closed physical system is described by the Hermitian Hamiltonian, H_S . Then, Let us assume that it can interact with its environment and thus becomes an non-Hermitian system (open system). The resulting non-Hermitian system can be described by a non-Hermitian Hamiltonian formulated by

$$H_{\text{NH}} = H_S + V_{SE}G_E^{(\rightarrow)}V_{ES}, \quad (1)$$

where $G_E^{(\rightarrow)}$ is an outgoing Green function in an environment and V_{SE} (V_{ES}) is the interaction between the environment (the closed system) and closed system (the environment) [10]. Considering two specific interacting eigenstates with negligible interaction with the other states, the non-Hermitian Hamiltonian can be modeled in a two-by-two matrix form as

$$H_{\text{NH}} = \begin{pmatrix} S_{11} + E_{11} & S_{12} + E_{12} \\ S_{21} + E_{21} & S_2 + E_{22} \end{pmatrix}, \quad (2)$$

where S_{ij} is the matrix representation of H_S and E_{ij} is that of $V_{SE}G_E^{(\rightarrow)}V_{ES}$ with respect to the eigenbasis of H_S . Here, S_{ij} ($i \neq j$) corresponds to the internal coupling, E_{ij} ($i = j$) are self-energies (i.e., interaction with the environment itself), and E_{ij} ($i \neq j$) are called collective Lamb shifts (i.e., interaction via the environment). For convenience, we set $S_{ij} + E_{ij}$ ($i = j$) to $\xi_i \in \mathbb{C}$ and $S_{ij} + E_{ij}$ ($i \neq j$) to $g \in \mathbb{C}$. Thus, the eigenvalues of the non-Hermitian Hamiltonian are given by:

$$\lambda_{\pm} = \frac{\xi_1 + \xi_2}{2} \pm \eta, \quad (3)$$

where $\eta = \sqrt{\frac{(\xi_1 - \xi_2)^2}{4} + g^2}$. Generally, it is assumed that the coupling constant $g \in \mathbb{C}$ is a Hermitian coupling under the strong real part, i.e., $g_{12} = g_{21}^*$ and $\text{Re}(g) > \text{Im}(g)$, and this toy model successfully addresses EPs related to $f(z) = z^{1/n}$ -type Riemann surfaces. Here, $N \in \mathbb{N}$ is an integer (typically $N = 2, 3$) and $z \in \mathbb{C}$. In this work, however, we extend g to be a non-Hermitian coupling under the strong imaginary part, i.e., $g_{12} \neq g_{21}^*$ and $\text{Im}(g) > \text{Re}(g)$. This extension supports the new features of a non-Hermitian Hamiltonian and new topological structures of Riemann surfaces.

PROPOSED PHYSICAL SYSTEM

Our non-Hermitian system in this paper is a two-dimensional elliptical optical microcavity with a major

axis a and a minor axis b . The axes are defined as $a = 1 + \chi$ and $b = \frac{1}{1 + \chi}$, respectively, as functions of the deformation parameter χ , ensuring a constant area of π . The refractive index outside the microcavity (n_{out}) is fixed at $n = 1$ (vacuum), while the refractive index of the cavity medium (n_{in}) is varied to determine the location of the EPs along with the deformation parameter χ in the parameter plane.

The eigenvalues and eigenfunctions are obtained by solving the Helmholtz equation $\nabla^2 \psi + n^2 k^2 \psi = 0$ using the boundary element method (BEM) [64]. This calculation is performed for transverse magnetic modes in the elliptical two-dimensional cavity in the x and y planes, where k is the wave number, and ψ is the z -component of the electric field.

In this work, we model the elliptical optical microcavity as an open system described by a non-Hermitian Hamiltonian. This model is well-suited for studying non-Hermitian effects, as the closed elliptical cavity is an integrable system with no avoided crossings, resulting in Poisson distributions [65, 66].

Accordingly, internal coupling S_{ij} ($i \neq j$) is not required, and the off-diagonal elements in Eq. (2) are simply E_{ij} ($i \neq j$). Thus, we consider avoided crossings solely as effects of openness

EXTENSION FROM HERMITIAN COUPLING TO NON-HERMITIAN COUPLING IN A TOY MODEL

In this section, the coupling g , which is typically defined as Hermitian coupling, is extended to non-Hermitian coupling in the form of a 2×2 non-Hermitian Hamiltonian toy model. To perform the calculations of the toy model, following Ref. [63], we set the real parts of ξ (i.e., ξ^r) as a function of α as $\xi_1^r(\alpha) = 1 - \frac{\alpha}{2}$ and $\xi_2^r(\alpha) = \sqrt{\alpha}$, while the imaginary part of ξ (i.e., ξ^i) is fixed in the considered range of parameters. Moreover, the non-Hermitian coupling term g is exponentially sensitive to the relative difference between the two values (ξ_1, ξ_2), yielding the following form: $g(\alpha; \xi_1, \xi_2) = g_c \Lambda_\alpha(\xi_1, \xi_2)$. Here, g_c is the coupling coefficient and the sensitivity $\Lambda_\alpha(\xi_1, \xi_2)$ is defined as $\Lambda_\alpha(\xi_1, \xi_2) = \exp[-\{\xi_1(\alpha) - \xi_2(\alpha)\}^2]$ [63]. In general, the coupling coefficient g_c is complex.

Comparison between Landau-Zener interaction and width bifurcation

To validate the effects of transition from Hermitian to non-Hermitian coupling, especially to examine the role of the ratio between the real and imaginary parts, we simultaneously study the typical Landau-Zener avoided crossing and the lesser-known width bifurcation, which

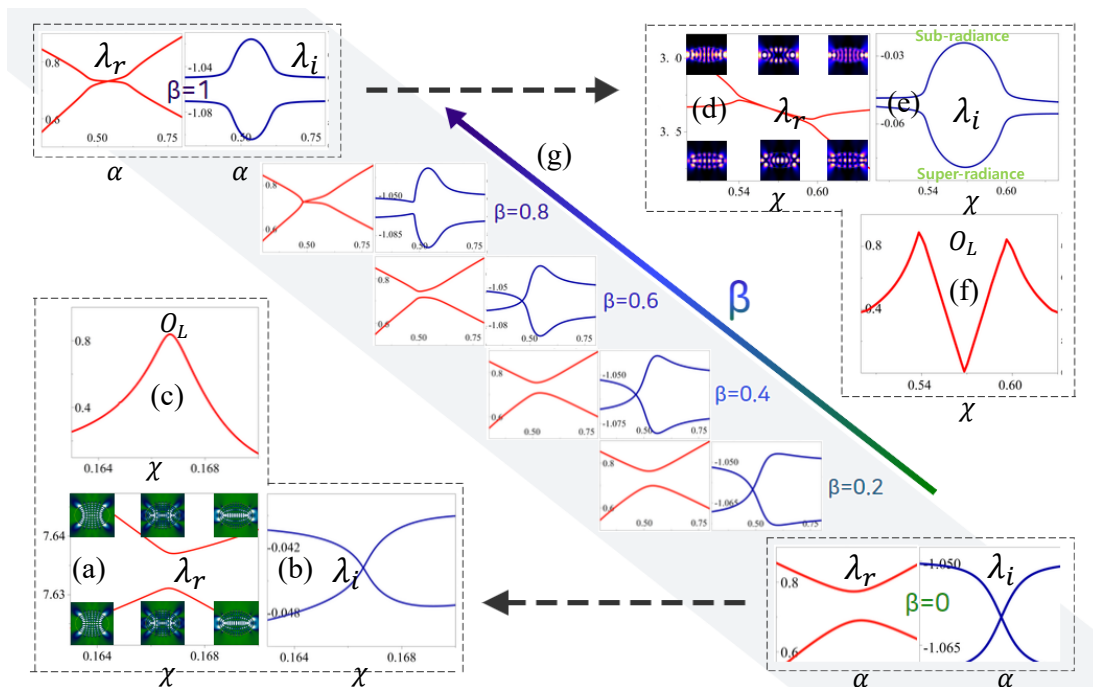


FIG. 1: Typical Landau-Zener avoided crossing (lower left panels) vs. width bifurcation (upper right panels). Insets display intensity plots of eigenstates corresponding to the eigenvalues. (a) The real parts of eigenvalues exhibit avoided crossing with eigenstate exchange. (b) The imaginary parts of eigenvalues display mode crossing. (c) The overlap integral of two interacting eigenstates is maximized near the center of the avoided crossing. (d) The real parts of eigenvalues show a crossing. (e) The imaginary parts of eigenvalues bifurcate around two critical points. (f) The overlap integral of two interacting eigenstates is maximized near the edges of the bifurcations. (g) The transition from Landau-Zener avoided crossing to width bifurcation is shown as a function of β .

involves both super-radiance and sub-radiance. Lower panels (a), (b), and (c) in Fig. 1 correspond to Landau-Zener avoided crossing [67, 68], whereas the upper panels (d), (e), and (f) in Fig. 1 correspond to width bifurcation [62, 63]. Around $\chi \simeq 0.167$, the real parts of eigenvalues, λ_r , in Fig. 1(a) exhibit an avoided crossing with an exchange of eigenstates, while the imaginary parts of the eigenvalues, λ_i , in Fig. 1(b) show the crossing. The insets in Fig. 1(a) show the intensity plots of the eigenfunctions corresponding to each eigenvalue. Furthermore, to study the relation with EPs, we consider the overlap integrals of two interacting eigenstates defined as follows:

$$O_L(i, j) = \frac{1}{X_i X_j} \iint dxdy |\psi_i^*(x, y) \psi_j(x, y)|, \quad (4)$$

where $X_i = \sqrt{\int dxdy |\psi_i(x, y)|^2}$ denotes the normalization factor.

The result for the Landau-Zener avoided crossing is presented in Fig. 1(c), with its value maximized around the center of the avoided crossing ($\chi \simeq 0.167$). These behaviors directly indicate that the EP is located around $\chi \simeq 0.167$. In contrast, the width bifurcation (upper panels) shows significantly different behavior. First, the real parts of the complex eigenvalues (λ_r) cross each other,

and interestingly, the real parts (λ_r) remain together in finite parameter regions. This behavior is distinct from the Landau-Zener interactions, which exhibit avoided crossing in narrow regions. The insets in Fig. 1(d) show the intensity plots of the eigenfunctions corresponding to each eigenvalue. The imaginary parts of the complex eigenvalues (λ_i) reveal more intriguing phenomena, such as bifurcation of the λ_i 's around two critical points, with the relative difference between these two λ_i 's maximized at the center of the bifurcation. The dramatic increase (or decrease) in decay is known as super-radiance (sub-radiance) in quantum optics [63, 69]. In Fig. 1(f), the overlap integral of the two interacting eigenstates O_L is maximized around the two edges of the bifurcations. As mentioned previously, these two peak values indicate that there are two EPs around these two peaks.

Based on these observations, the lower left panels, associated with the Landau-Zener interaction, and the upper right panels, associated with the width bifurcation, exhibit highly distinctive features. This distinction suggests that these phenomena arise from different physical mechanisms and cannot be directly related. However, extending the framework from Hermitian coupling to non-Hermitian coupling offers a resolution to this issue. In this approach, we introduce a complex coefficient (g) as

a convex combination of its real and imaginary parts, expressed in the following form:

$$g(\alpha, \beta) = g_c [(1 - \beta) + \iota\beta] \Lambda_\alpha(\xi_1, \xi_2), \quad (5)$$

where $g \in \mathbb{C}$, $g_c, \beta \in \mathbb{R}$, $\iota = \sqrt{-1}$, and $0 \leq \beta \leq 1$.

By employing $g(\alpha, \beta)$, we calculate the eigenvalues (λ_\pm) with the initial values of $g_c = 0.043$, $\xi_1^i = 1.05$, $\xi_2^i = 1.07$, and the results are shown in Fig. 1(g). The results show a smooth transition from the Landau–Zener interaction to width bifurcation as a function of increasing β . The coupling g is a pure real value at $\beta = 0$, and it corresponds to Landau–Zener interactions, as shown in Fig. 1(a) and (b). At $\beta = 0.8$, λ_r s are crossed, and λ_i s clearly exhibit a width bifurcation. When β reaches a value 1, the coupling g becomes a pure imaginary value, which corresponds to the width bifurcation, as shown in Fig. 1(d) and (e).

In this way, the Landau-Zener interaction can be smoothly transformed to width bifurcation by exploiting the non-Hermitian coupling coefficient under a convex combination of the real and imaginary parts.

SUCCESSIVE TRANSITIONS OF AVOIDED CROSSINGS IN A MICROCAVITY AND TOY MODEL

We identified a pair of EPs analytically in the non-Hermitian Hamiltonian toy model described in the previous section for a simple case. However, the analytical solutions of the non-Hermitian Hamiltonian matrix elements are not explicitly known in microcavities, which are common in conventional open physical systems. Hence, we rely on numerical methods to specify the locations of the EPs. A good strategy can be coarse scanning a parameter plane until the transition of the avoided crossing occurs, because the EP is a singular point where the transition between strong and weak interactions occurs [60, 61]. Thus, an avoided crossing of the real part with the crossing of the imaginary part is converted into an avoided crossing of the imaginary part with the crossing of the real part when going across the EPs and vice versa.

Consequently, we found five representative classes in both the BEM and toy models, as shown in Fig. 2. The left panels are the eigenvalue trajectories obtained from our BEM simulation, whereas the right panels are the eigenvalue trajectories obtained from the toy model Hamiltonian for some specific parameters (shown in Table I). For the BEM, we obtained the eigenvalues by scanning the deformation parameter χ in the range of $0.05 \leq \chi \leq 0.63$ at each fixed n_{in} . Note that these two panels show similar behavior in each class. Five representative classes were classified to capture the transition of avoided crossing. Class 1 corresponds to the avoided crossing of the real part: (1-a) and (1-c), and the crossing

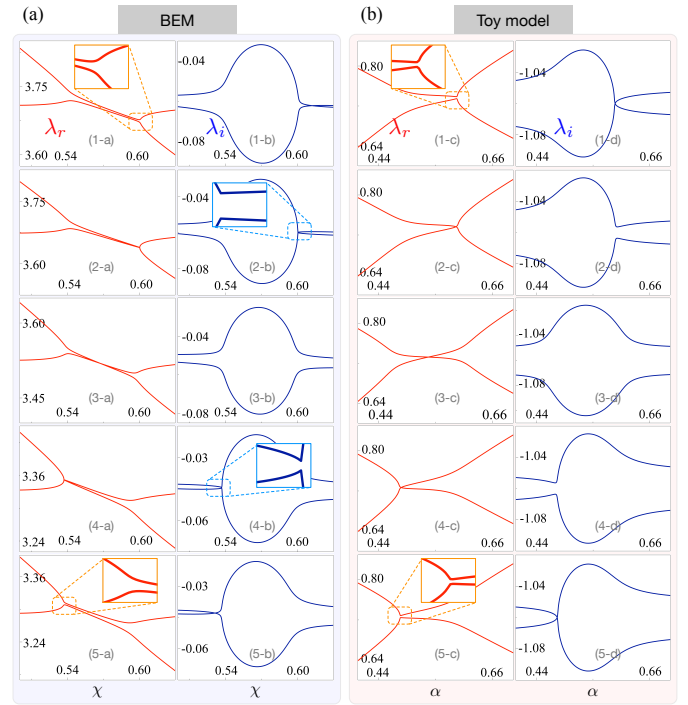


FIG. 2: Some representative eigenvalue trajectories according to Table I. Left panels are eigenvalue trajectories obtained from our BEM simulation. Right panels are eigenvalue trajectories obtained from the toy model Hamiltonian. Both panels show similar behavior.

of the imaginary part: (1-b) and (1-d). On the contrary, Classes 2, 3, and 4 correspond to the avoided crossing of the imaginary part: (2-b, 3-b, 4-b) and (2-d, 3-d, 4-d), with the crossing of the real part: (2-a, 3-a, 4-a) and (2-c, 3-c, 4-c). Finally, Class 5 again corresponds to the avoided crossing of the real part: (5-a) and (5-c), with the crossing of the imaginary part: (5-b), (5-d). Importantly, for the left panels (BEM), a careful examination reveals that the transitions of avoided crossing occur around two critical points at $\chi \simeq 0.6$ and $\chi \simeq 0.53$, respectively. These two critical points correspond to the a pair of EPs.

For a deeper understanding of these phenomena, we present some representative parameters for the successive transition of avoided crossing in both the microcavity and toy models. Since the refractive index n_{in} only increases as the class number increases, we can hardly obtain any meaningful information related to the transition of the avoided crossing in the BEM simulations. However, various parameters of the toy model can provide useful physical information. First, these types of transitions can occur when the imaginary part of the complex coefficient of coupling is larger than the real part of the complex coefficient of coupling throughout the process. This condition is essential for maintaining the structure of the width bifurcation, as shown in Fig. 1(g). It should be noted that the key to successive transitions of the avoided crossings

	n_{in}	g_c	β	γ_1	γ_2	λ_r	λ_i
Class 1	2.6	0.043	0.76	1.05	1.07	A.C.	C.
Class 2	2.6257	0.043	0.78	1.05	1.07	C.	A.C.
Class 3	2.74	0.043	1	1.05 (1.07)	1.07 (1.05)	C.	A.C.
Class 4	2.9036	0.043	0.78	1.07	1.05	C.	A.C.
Class 5	2.94	0.043	0.76	1.07	1.05	A.C.	C.

TABLE I: Some representative parameters for successive transitions of the avoided crossings in the microcavity and toy model. Class 1 corresponds to the avoided crossing of λ_r with crossing of λ_i . Class 2, 3 and 4 correspond to the avoided crossing of λ_i with crossing of λ_r . Class 5 corresponds to the avoided crossing of λ_r with crossing of λ_i .

is related to the crossover of the critical value of β_c in the range $0.76 \leq \beta \leq 0.78$. In our examples, the value of β_c was approximately 0.765. Therefore, Class 1 has β less than β_c . The value of β is larger than β_c in Class 2, and increases until $\beta = 1$ in Class 3. Then, β decreases towards β_c in Class 4. In Class 5, it becomes smaller than β_c . Moreover, the relative magnitude of γ_i determines the crossover position. When $\gamma_2 > \gamma_1$, crossover occurs at approximately $\alpha = 0.61$, whereas for $\gamma_1 > \gamma_2$, crossover occurs approximately $\alpha = 0.52$.

RIEMANN SURFACES FOR A PAIR OF EPS IN AN OPTICAL MICROCAVITY

We analyzed the successive transitions associated with the five representative avoided crossings in the range of $0.5 \leq \chi \leq 0.63$ and $2.6 \leq n \leq 2.94$, and verified the two critical points around $n \simeq 2.6257, \chi = 0.601$ and $n \simeq 2.9036, \chi = 0.53$. Accordingly, by obtaining the whole eigenvalue trajectories by scanning the parameter plane that includes this range, we obtain new topological structures of the a pair of EPs. To display the topological structured of a pair of EPs more clearly, we consider the relative differences $\Delta\lambda_{\pm}$ from the eigenvalues λ_{\pm} with respect to their mean values $\lambda_{\text{AV}} = \frac{\lambda_+ + \lambda_-}{2}$ instead of the eigenvalue λ_{\pm} : $\Delta\lambda_{\pm} = \lambda_{\pm} - \lambda_{\text{AV}}$. In this way, the Riemann surfaces of the real parts are displayed in Fig. 3(a), whereas those of the imaginary parts are shown in Fig. 3(b). The pair of EPs is located at $(n \simeq 2.6257, \chi = 0.6001)$ and $(n \simeq 2.9036, \chi = 0.5372)$, respectively. Moreover, the branch cut of the Riemann surfaces for the real parts is a curve directly joining these two EPs, whereas that for the imaginary part is the two curves in the outward direction to the branch cut of the Riemann surfaces for real parts. Accordingly, we immediately notice that their topological structures are manifestly different from that of typical Riemann surfaces, such as $f(z) = (z - z_0)^{1/N}$. It can be argued that the Riemann surfaces shown in Fig. 3 have topological structures equivalent to the following function:

$$f(z) = \sqrt{(z - z_1)(z - z_2)}, \quad (6)$$

where $z_1 \neq z_2$.

This argument is supported by the topological equivalence between the Riemann surfaces shown in Fig. 3(c) and (d), plotted using *Mathematica* based on the function $f(z) = \sqrt{(z - z_1)(z - z_2)} = w$ with $z_1 = i$ and $z_2 = -i$, and the Riemann surfaces shown in Fig. 3(a) and (b).

Precisely, we identify a parameter plane $\mathbb{P} = \{(n, \chi) : n, \chi \in \mathbb{R}\}$ with the complex plane \mathbb{C} by an orientation preserving homeomorphism $\rho : \mathbb{P} \rightarrow \mathbb{C}$ with $\rho(\text{EP}_1) = z_1$ and $\rho(\text{EP}_2) = z_2$. This mapping establishes a direct association between EPs in the parameter space and branch points in the complex plane.

Then, ρ induces a conformal structure to \mathbb{P} . We can lift the conformal structure onto the Riemann surface S_r so that the projection ϕ from Riemann surface to parameter space \mathbb{P} in Fig. 3 is a holomorphic function under the conformal structure. Moreover, by the classical results of the Riemann surface theory, ϕ is realized as some restriction of the coordinate projection $p_1 : \mathbb{C} \times \mathbb{C} \rightarrow \mathbb{C}$ defined by $p_1(z, \omega) = z$. To see this, by using the classical result of the Riemann surface theory, we can find a polynomial $F(z, \omega)$ in $\mathbb{C}[z][[\omega]]$ so that

$$\mathcal{Z}(F) = \{(z_0, \omega_0) \in \mathbb{C} \times \mathbb{C} : F(z_0, \omega_0) = 0\} \quad (7)$$

is S_r and $p_1|_{\mathcal{Z}(F)} = \phi$. Indeed, we may set

$$F(z, \omega) = \omega^2 - (z - z_1)(z - z_2).$$

In particular, such a $\mathcal{Z}(F)$ is called a cyclic covering of the projective line.

In order to characterize the location of EPs in terms of critical points, we consider $\partial_{\omega} F(z_0, \omega_0) = 2\omega_0 = 0$ known as critical point or bifurcation point. It means that there are branches of the $\mathcal{Z}(F)$ on the side of z when z varies. Hence, the preimage of the a pair of EPs under ϕ are located at $(i, 0)$ and $(-i, 0)$ where each $\partial_z F$ does not vanish.

To see branching at $(i, 0)$ and $(-i, 0)$, we take a biholomorphic function ψ_+ from a small neighborhood D_+ of 0 to a small neighborhood of i so that $F(\psi_+(\omega), \omega) = 0$ for all $\omega \in D_+$. Likewise, we can also take a biholomorphic function ψ_- defined on a small neighborhood D_- of 0. By simple computations and by using the condition that

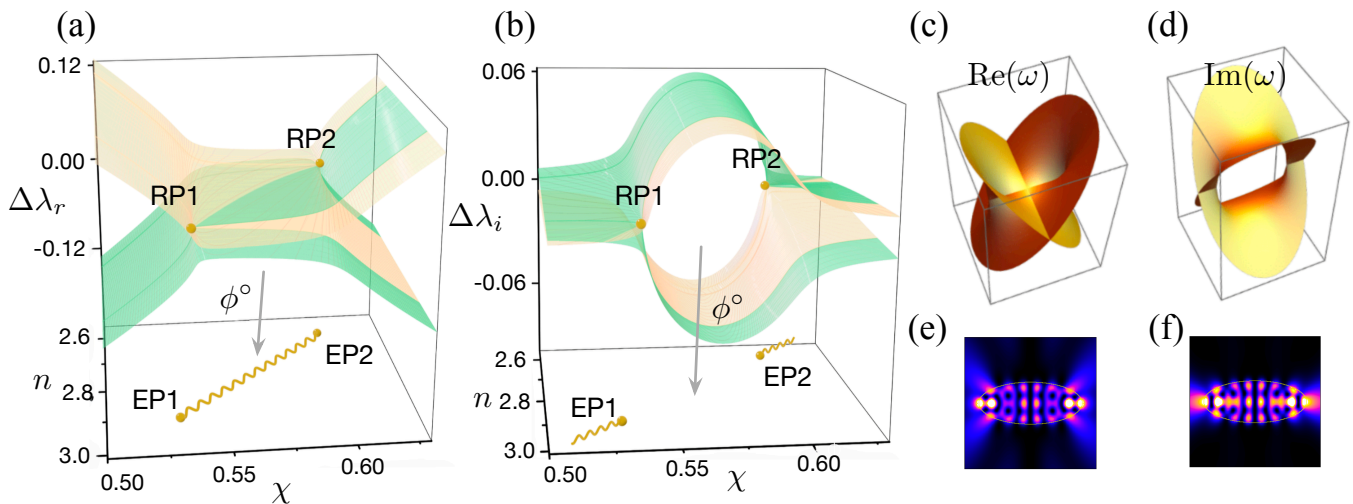


FIG. 3: Riemann surfaces (covering space) of the pair of EPs in an optical microcavity are displayed in the parameter plane (base space). The Riemann surface of real part is shown in (a), while that of imaginary parts is presented in (b). Both surfaces are projected onto the base space through the covering map ϕ° . The pair of EPs are located at $n \simeq 2.6257, \chi = 0.601$, and $n \simeq 2.9036, \chi = 0.53$, respectively. The figures (c) and (d) are plotted using *Mathematica* from the function $f(z) = \sqrt{(z - z_1)(z - z_2)} = w$. The figures (e) and (f) are intensity plots of eigenfunctions at EP₁ and EP₂, respectively.

$F(\psi_\pm(\omega), \omega) = 0$, we can obtain that the Taylor expansion of $z = \psi_\pm(\omega)$ near $\omega = 0$ is

$$\psi_\pm(\omega) = \pm i \mp \frac{i}{2}\omega^2 + O(\omega^3), \quad (8)$$

respectively.

For more strict mathematical structure of Riemann surfaces, we need to invoke the covering theory, which is essential to study the relation between Riemann surfaces (covering space) and their projected plane (base space) on the bottom. In fact, our surface $\mathcal{Z}(F)$ is a Galois branched covering for \mathbb{C} . In general, given a proper holomorphic map $\phi: Y \rightarrow X$ between Riemann surfaces Y (branched covering space) and X (base space), the collection S_ϕ of all points in Y , at which ϕ fails to be a local homeomorphism, is a discrete and closed subset of Y . Each element in S_ϕ is called a *ramification point* (RP). Then, the restriction and corestriction ϕ° of ϕ to $Y^\circ = Y \setminus \phi^{-1}(\phi(S_\phi))$ and onto $X^\circ = X \setminus \phi(S_\phi)$, respectively, is an (unbranched) covering. In our case, we can say that $S_\phi = \{\text{RP}_1, \text{RP}_2\}$ and the mapping ϕ maps RP_{*i*} to EP_{*i*}.

Also, when the explicit form of the covering space Y is given by the zero locus $\mathcal{Z}(P)$ for some complex polynomial $P \in \mathbb{C}[z][[\omega]]$ as above, the (unbranched) covering map ϕ° is the projection p_1 to the first coordinate, namely, $p_1: \mathcal{Z}(P) \rightarrow \mathbb{C}$ with $p_1(z, \omega) = z$.

More importantly, for each $a \in Y$, the local expression of ϕ° near a is given by $\tilde{\psi} \circ \phi^\circ \circ \tilde{\varphi}^{-1}(v) = v^{e_a}$ for some local coordinates $\tilde{\varphi}, \tilde{\psi}$ and for some positive integer e_a .

Here, e_a does not depend on the local coordinates and it depends only on a . We call e_a the *ramification index* of ϕ at a .

In our case, the $\psi_\pm(\omega)$ play the role of the local covering map at a . Hence, it follows from Eq.8 that the our (unbranched) covering has its *ramification index* $e_{\text{RP}} = 2$ at each ramification point RP. In fact, our covering is a *Galois* covering and so for each $x \in X$, every point in $\phi^{-1}(x)$ has same ramification index. Therefore, we can define the *order* of x as e_y for some $y \in \phi^{-1}(x)$.

Path Lifts and corresponding braid Structures for a pair of exceptional points

Using the well-known unique path lifting property, we can unify the relationship between the paths on Riemann surfaces and the braid structure as follows. When $\phi: Y \rightarrow X$ is a (branched) covering as above and $\alpha: I = [0, 1] \rightarrow X^\circ$ is any path on the base space, avoiding $\phi(S_\phi)$, for each $p \in \phi^{-1}(\alpha(0))$, there exists a unique map $\tilde{\alpha}: [0, 1] \rightarrow Y^\circ$ such that $\tilde{\alpha}(0) = p$ and $\phi \circ \tilde{\alpha} = \alpha$, that is, the following diagram commutes:

$$\begin{array}{ccc} & Y & \\ & \nearrow \tilde{\alpha} & \downarrow \phi \\ I & \xrightarrow{\alpha} & X \end{array}$$

In our case, the covering spaces (Riemann surfaces) are denoted as Y_{R} for the real part and Y_{I} for the imaginary part, with a common base space X representing the parameter space. According to the four control loops $\alpha_{i=1,2,3,4}$, based at $\alpha_i(0) = \alpha_i(1) = x_0 \in X$, and its fibers $\phi^{-1}(x_0) = \{y_a, y_b\}$, the 16 lifted paths on each Riemann surface are shown in Fig. 4. More precisely, choose

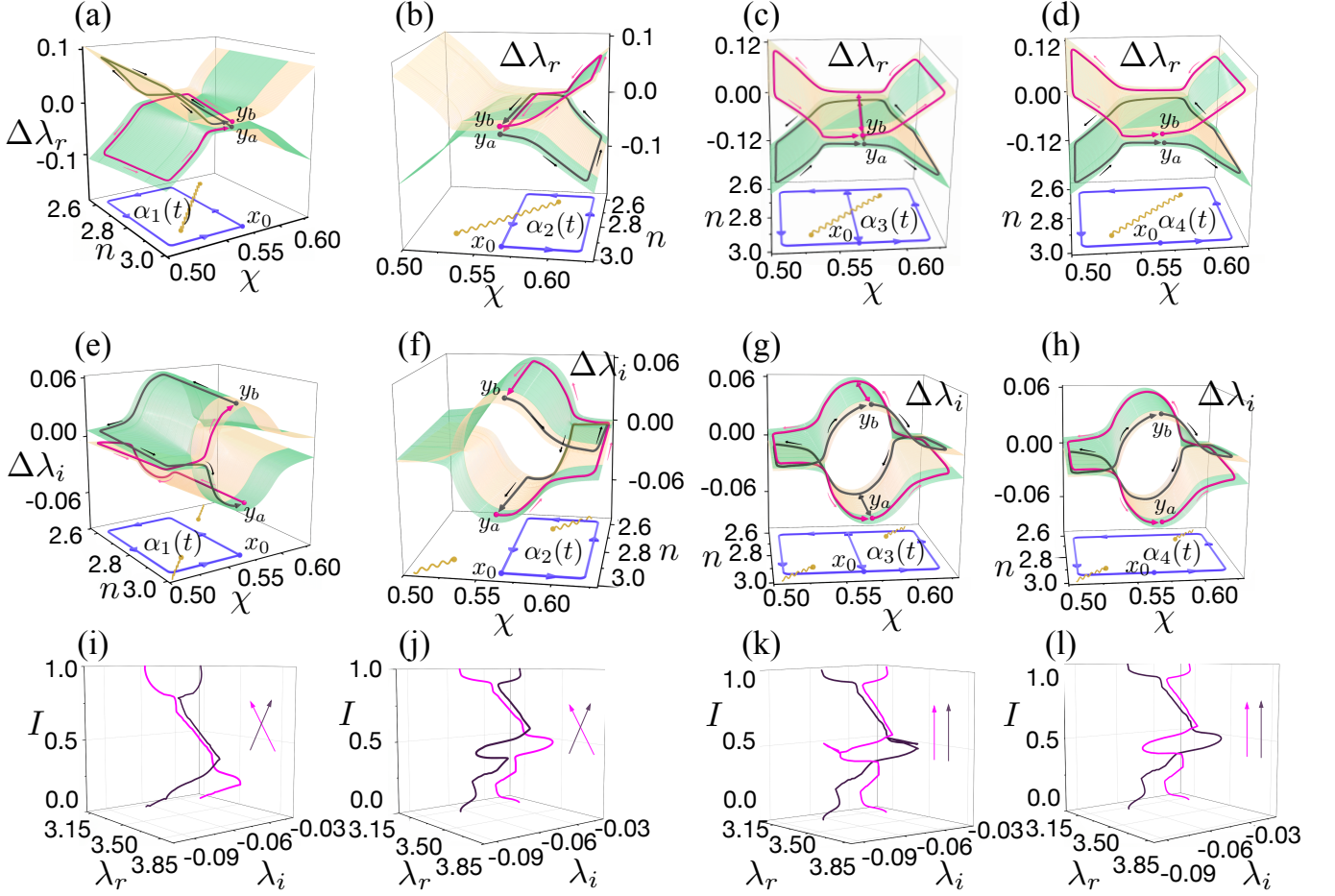


FIG. 4: Path lifts on the Riemann surfaces (covering space) from the parameter space (base space) and the corresponding braids constructed from them. The base point of the control loop in the parameter space is x_0 , and its corresponding fibers on the Riemann surfaces are y_a, y_b . (a) Control loop α_1 encircling EP_1 and its corresponding path lift on the Riemann surfaces for the real part and the imaginary part (e). (b) Control loop α_2 encircling EP_2 and its corresponding path lift on the Riemann surfaces for the real part and the imaginary part (f). (c) Loop α_3 encircling EP_1 and EP_2 individually, with its corresponding path lift on the Riemann surfaces for the real part and the imaginary part (g). (d) Control loop α_4 encircling EP_1 and EP_2 simultaneously, with its corresponding path lift on the Riemann surfaces for the real part and the imaginary part (h). (i)–(l): Braids obtained from the path lifts for the control loops $\alpha_1, \alpha_2, \alpha_3$, and α_4 , respectively.

$i \in \{1, 2, 3, 4\}$. Then, α_i has unique lifts $\tilde{\alpha}_R^a(t)$ and $\tilde{\alpha}_I^a(t)$ to Y_R and Y_I , respectively, starting at y_a . Likewise, there are unique lifts $\tilde{\alpha}_R^b(t)$ and $\tilde{\alpha}_I^b(t)$ to Y_R and Y_I , respectively, starting at y_b . Using these conventions, we can define two parametric curves on \mathbb{C} as:

$$\lambda^a(t) = \tilde{\alpha}_R^a(t) + i\tilde{\alpha}_I^a(t) \in \mathbb{C}, \quad \lambda^b(t) = \tilde{\alpha}_R^b(t) + i\tilde{\alpha}_I^b(t) \in \mathbb{C}.$$

These curves naturally define a braid in the topological space $S_{0,3} = \mathbb{C} \setminus \{\lambda_{EP_1}, \lambda_{EP_2}\}$. To see this, we briefly introduce the braid group of $S_{0,3}$. The configuration space $\text{UConf}_2(S_{0,3})$ of unordered 2 points in $S_{0,3}$ is defined as follows:

$$\text{UConf}_2(S_{0,3}) = \{(z, w) \in S_{0,3} \times S_{0,3} \mid z \neq w\} / (z, w) \sim (w, z)$$

where $(z, w) \sim (w, z)$ means that we identify (z, w) with (w, z) . The *second braid group* or *braid group with 2*

strands of $S_{0,3}$ is defined as the fundamental group of $\text{UConf}_2(S_{0,3})$:

$$B_2(S_{0,3}) \doteq \pi_1(\text{UConf}_2(S_{0,3})).$$

Using this definition, we can see that the map $\beta : I \rightarrow \text{UConf}_2(S_{0,3})$ defined by

$$t \mapsto (\lambda^a(t), \lambda^b(t))$$

is a braid in $B_2(S_{0,3})$. Clearly, the exchange of the 2 strands is confirmed by considering a loop in $\text{UConf}_2(T)$:

$$\begin{aligned} \beta(t=0) &= (\lambda^a(0) = z_0, \lambda^b(0) = w_0), \\ \beta(t=1) &= (\lambda^a(1) = w_0, \lambda^b(1) = z_0). \end{aligned} \quad (9)$$

Our results related to the pair of EPs are shown in Fig. 4. Control loops α_1 and α_2 , which encircle EP_1 and

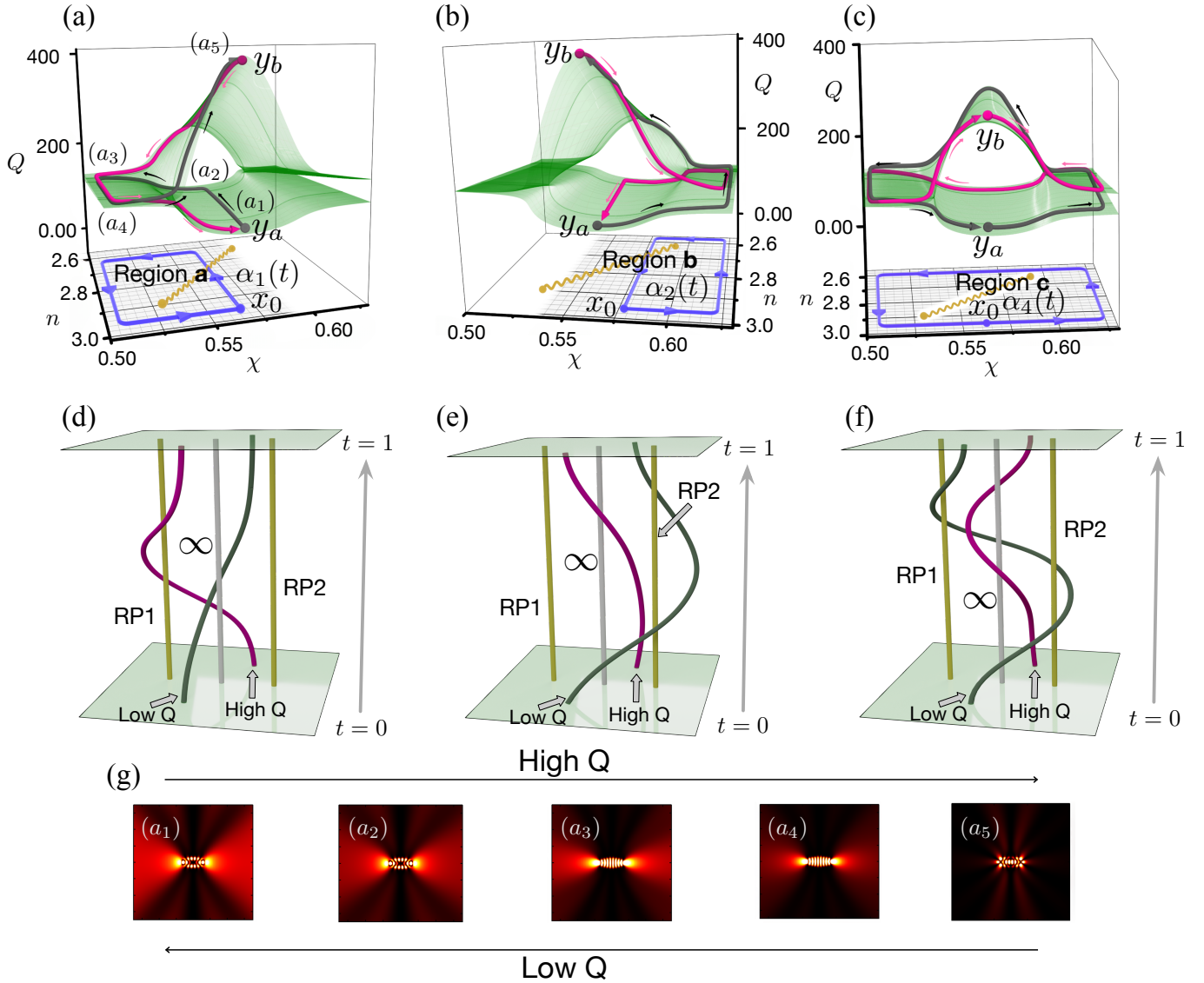


FIG. 5: Topologically protected Q-switching supported by a pair of EPs. Any loop homotopic to α_1 (in region **a**) or α_2 (in region **b**) leads to Q-switching. In contrast, any loop homotopic to α_4 in region **c** does not lead to Q-switching. Any isotopic braid to the given strands (cyan, yellow) in (d) and (e) results in Q-switching, whereas any isotopic braid to the given strands (cyan, yellow) in (f) does not result in Q-switching.

EP₂ respectively, along with their corresponding path lifts on the Riemann surfaces for the real and imaginary parts, are shown in (a) and (e) ((b) and (f)). Similarly, control loops α_3 and α_4 , which encircle EP₁ and EP₂ individually (simultaneously), along with their corresponding path lifts on the Riemann surfaces for the real and imaginary parts, are shown in (c) and (g) ((d) and (h)), respectively.

The figures (i), (j), (k), and (l) depict the braids obtained from the path lifts for the control loops α_1 , α_2 , α_3 , and α_4 , respectively. These figures clearly show that the braids for the control loops α_1 and α_2 induce eigenvalue switching, whereas the braids for α_3 and α_4 do not.

Notably, the braid for α_3 in Fig. 4(k) is isotopic to the braid for α_4 in Fig. 4(l). An homotopy between the control loops α_3 and α_4 explains an isotopy observed in the braids depicted in Fig. 4(k) and Fig. 4(l).

Topologically protected Q-switching supported by the pair of EPs

The quality factor Q is a fundamental parameter in resonant systems, characterizing the sharpness of resonance and the efficiency of energy storage relative to energy dissipation. Generally, Q is defined as the ratio of the resonant frequency to the bandwidth or, equivalently, the

ratio of energy stored to energy lost per cycle. In practical implementations, Q-switching techniques typically rely on modulating the gain or loss in a resonator, often requiring precise control of non-adiabatic transitions or external perturbations. These methods, while effective, are constrained by stringent experimental requirements, such as high-speed modulation, synchronization, or material-specific limitations, which can introduce challenges in scalability and robustness. In contrast, our approach leverages a topologically protected mechanism for Q-switching, utilizing a pair of exceptional points (EPs) exhibiting superradiance and subradiance. This method eliminates the need for non-adiabatic transitions and chiral behavior, thus is inherently robust against noise and system imperfections, offering a more flexible and reliable solution for Q-switching in resonant systems.

More precisely, Fig. 5(a), (b), and (c) illustrate the covering space Y_Q for the quality factor Q , calculated as $Q = \frac{\lambda_r}{2|\lambda_i|}$. This result is obtained from the covering spaces Y_R and Y_I , which correspond to the real and imaginary parts of the complex eigenvalues, respectively. The covering space Y_Q is topologically equivalent to the plane with one point removed. For instance, see the bottom plane in Fig. 5(d), which is the flattened Y_Q . In this plane, the two intersection points with the two yellow strands are RP_1 and RP_2 , while the intersection point with the white strand represents the deleted point. We observe that any control loop homotopic to α_1 in region **a** in (a) or α_2 in region **b** in (b), based at x_0 , leads to the exchange of fibers $\{y_a, y_b\} \in Y_Q$.

In contrast, any control loop homotopic to α_4 in region **c** in (c) does not result in the exchange of fibers $\{y_a, y_b\} \in Y_Q$. This observation is directly associated with the switching behavior of braids as shown in Fig. 5(d) and (e). The braids in Fig. 5(d), (e) and (f) are given by lifted paths α_i^a and α_i^b of each α_i to Y_Q , starting at y_a and y_b . To see this, as in the previous section, we consider the configuration space $\text{UConf}_2(Y_Q^\circ)$ of unordered pairs of points in $Y_Q^\circ = Y_Q \setminus \{RP_1, RP_2\}$. Then, the isotopy class of the curve defined by $t \mapsto (\alpha_i^a(t), \alpha_i^b(t))$ is a braid in

$$B_2(Y_Q^\circ) \doteq \pi_1(\text{UConf}_2(Y_Q^\circ)).$$

Moreover, the orientation of encircling the EPs is irrelevant, as the exchange of Q-values occurs independently of the braiding direction; This implies that the chirality is not a necessary condition for the exchange of Q-values. This behavior demonstrates a topologically protected Q-switching mechanism, where all control loops within regions **a** and **b** induce Q-switching, regardless of the specific paths or chirality, while any control loops in region **c** do not exhibit such switching. In addition, Fig. 5(g) shows the series intensity plot of the resonance mode from a_1 to a_5 , as marked in Fig. 5(a).

CONCLUSIONS

In this study, we have emphasized the critical importance of the Q-switching in optical microcavity laser. Despite its significance, conventional Q-switching methods often face challenges in practical implementation due to their sensitivity to environmental disturbances and noise, which can destabilize the system and degrade performance.

To address these limitations, we proposed a novel approach leveraging the non-trivial topological structure of a pair of EPs formed through super-radiance and sub-radiance. This framework enables the realization of topologically protected Q-switching, which is inherently robust and resistant to external disturbances and noise. The robustness of this mechanism arises from the homotopic properties of control loops in the parameter space, which are equivalently described by the isotopy properties of braid groups for Riemann surfaces.

This topological protection ensures that the Q-switching process remains stable and reliable, even in the presence of perturbations, thereby overcoming the practical challenges associated with traditional methods. Our findings pave the way for designing resilient laser systems and provide a foundation for further exploration of topological phenomena in laser physics and beyond.

ACKNOWLEDGMENTS

This work was supported by the National Research Foundation of Korea (NRF) through a grant funded by the Ministry of Science and ICT (RS-2023-00211817, RS-2022-NR072395, NRF-2022M3H3A1098237), the Institute for Information & Communications Technology Promotion (IITP) grant funded by the Korean government (MSIP) (No. 2019-0-00003; Research and Development of Core Technologies for Programming, Running, Implementing, and Validating of Fault-Tolerant Quantum Computing Systems), and Korea Institute of Science and Technology Information.

Disclosures

The authors declare no conflicts of interest.

Author Contributions

K.-W.P. proposed the study and performed theoretical analysis. K.K. performed the theoretical and mathematical analysis. K.J. supervised the overall investigation. K.-W.P., K.K., J.K., M.C., and K.J. wrote the

manuscript. K.-W.P. and K.K. contributed equally to this work.

* Electronic address: parkkw7777@gmail.com

† Electronic address: kyeongrokim14@gmail.com

‡ Electronic address: kgjeong6@snu.ac.kr

- [1] Y. Ando and L. Fu, “Topological Crystalline Insulators and Topological Superconductors: From Concepts to Materials,” *Annu. Rev. Condens. Matter Phys.* **6**, 361 (2015).
- [2] M. Z. Hasan and C. L. Kane, “Topological Insulators,” *Rev. Mod. Phys.* **82**, 3045 (2010).
- [3] Y. J. Chen *et al.*, “Observation of Topological Superconductivity in a Stoichiometric Transition Metal Dichalcogenide,” *Nat. Commun.* **12**, 1 (2021).
- [4] C. Nayak, S. H. Simon, A. Stern, M. Freedman, and S. Das Sarma, “Non-Abelian Anyons and Topological Quantum Computation,” *Rev. Mod. Phys.* **80**, 1083 (2008).
- [5] B. J. Brown, N. P. Breuckmann, and D. E. Browne, “Logical Blocks for Fault-Tolerant Topological Quantum Computation,” *PRX Quantum* **4**, 020303 (2023).
- [6] S. Barik, A. Karasahin, C. Flower, *et al.*, “A topological quantum optics interface,” *Science* **359**, 666 (2018).
- [7] L. Lu, J. D. Joannopoulos, and M. Soljačić, “Topological photonics,” *Nat. Photonics* **8**, 821 (2014).
- [8] A. Manchon, H. C. Koo, J. Nitta, *et al.*, “Spin-Orbitronics: A New Field Combining Spintronics and Topology,” *Nat. Mater.* **14**, 871 (2015).
- [9] J. Han and L. Liu, “Topological Insulators for Efficient Spin-Orbit Torques,” *APL Mater.* **9**, 060901 (2021).
- [10] I. Rotter, “A non-Hermitian Hamilton operator and the physics of open quantum systems,” *J. Phys. A: Math. Theor.* **42**, 153001 (2009).
- [11] W. D. Heiss, “Exceptional points of non-Hermitian operators,” *J. Phys. A: Math. Gen.* **37**, 2455 (2004).
- [12] T. Kato, *Perturbation Theory for Linear Operators* (Springer, Berlin, 1966).
- [13] W. Gao, X. Li, M. Bamba, and J. Kono, “Continuous transition between weak and ultrastrong coupling through exceptional points in carbon nanotube microcavity exciton-polaritons,” *Nat. Photon.* **12**, 362 (2018).
- [14] L. M. de Lépinay, B. Pigeau, B. Besga, and O. Arcizet, “Eigenmode orthogonality breaking and anomalous dynamics in multimode nano-optomechanical systems under non-reciprocal coupling,” *Nat. Commun.* **9**, 1401 (2018).
- [15] W. Xiong, Z. Li, Y. Song, J. Chen, G.-Q. Zhang, and M. Wang, “Higher-order exceptional point in a pseudo-Hermitian cavity optomechanical system,” *Phys. Rev. A* **104**, 063508 (2021).
- [16] H. Zhou, C. Peng, Y. Yoon, C. W. Hsu, K. A. Nelson, L. Fu, J. D. Joannopoulos, M. Soljačić, and B. Zhen, “Observation of bulk Fermi arc and polarization half charge from paired exceptional points,” *Science* **359**, 1009 (2018).
- [17] C. F. Fong, Y. Ota, Y. Arakawa, S. Iwamoto, and Y. K. Kato, “Chiral modes near exceptional points in symmetry broken H1 photonic crystal cavities,” *Phys. Rev. Res.* **3**, 043096 (2021).
- [18] W. Chen, Ş. K. Özdemir, G. Zhao, J. Wiersig, and L. Yang, “Exceptional points enhance sensing in an optical microcavity,” *Nature* **548**, 192 (2017).
- [19] C. Wang, W. R. Sweeney, A. D. Stone, and L. Yang, “Coherent perfect absorption at an exceptional point,” *Science* **373**, 1261 (2021).
- [20] D. Zhang, X.-Q. Luo, Y.-P. Wang, T.-F. Li, and J. Q. You, “Observation of the exceptional point in cavity magnon-polaritons,” *Nat. Commun.* **8**, 1368 (2017).
- [21] H. Liu, D. Sun, C. Zhang, M. Groesbeck, R. Mclaughlin, and Z. V. Vardeny, “Observation of exceptional points in magnonic parity-time symmetry devices,” *Sci. Adv.* **5**, eaax9144 (2019).
- [22] Y. Choi, C. Hahn, J. W. Yoon, and S. H. Song, “Observation of an anti-PT-symmetric exceptional point and energy-difference conserving dynamics in electrical circuit resonators,” *Nat. Commun.* **9**, 2182 (2018).
- [23] R. El-Ganainy, K. G. Makris, M. Khajavikhan, Z. H. Musslimani, S. Rotter, and D. N. Christodoulides, “Non-Hermitian physics and PT symmetry,” *Nat. Phys.* **14**, 11 (2018).
- [24] L. Xiao, T. Deng, K. Wang, Z. Wang, W. Yi, and P. Xue, “Observation of Non-Bloch Parity-Time Symmetry and Exceptional Points,” *Phys. Rev. Lett.* **126**, 230402 (2021).
- [25] M. I. Afzal and Y. T. Lee, “Supersymmetrical bounding of asymmetric states and quantum phase transitions by anti-crossing of symmetric states,” *Sci. Rep.* **6**, 39016 (2016).
- [26] A. Bergman, R. Duggan, K. Sharma, M. Tur, A. Zadok, and A. Alù, “Observation of anti-parity-time-symmetry, phase transitions and exceptional points in an optical fibre,” *Nat. Commun.* **12**, 486 (2021).
- [27] T. Gao, G. Li, E. Estrecho, T. C. H. Liew, D. Comber-Todd, A. Nalitov, M. Steger, K. West, L. Pfeiffer, D. W. Snoke, A. V. Kavokin, A. G. Truscott, and E. A. Ostrovskaya, “Chiral Modes at Exceptional Points in Exciton-Polariton Quantum Fluids,” *Phys. Rev. Lett.* **120**, 065301 (2018).
- [28] H. Nasari, G. Lopez-Galniche, H. E. Lopez-Aviles, A. Schumer, A. U Hassan, Q. Zhong, S. Rotter, P. LiKamWa, D. N. Christodoulides, and M. Khajavikhan, “Observation of chiral state transfer without encircling an exceptional point,” *Nature* **605**, 256 (2022).
- [29] K.-W. Park, J. Kim, S. Moon, and K. An, “Maximal Shannon entropy in the vicinity of an exceptional point in an open microcavity,” *Sci. Rep.* **10**, 12551 (2020).
- [30] J. Wiersig, “Enhancing the Sensitivity of Frequency and Energy Splitting Detection by Using Exceptional Points: Application to Microcavity Sensors for Single-Particle Detection,” *Phys. Rev. Lett.* **112**, 203901 (2014).
- [31] R. Kononchuk, J. Cai, F. Ellis, R. Thevamaran, and T. Kottos, “Exceptional-point-based accelerometers with enhanced signal-to-noise ratio,” *Nature* **607**, 697 (2022).
- [32] M. J. Grant and M. J. F. Digonnet, “Rotation sensitivity and shot-noise-limited detection in an exceptional point coupled-ring gyroscope,” *Opt. Lett.* **46**, 2936 (2021).
- [33] M. P. Hokmabadi, A. Schumer, D. N. Christodoulides, and M. Khajavikhan, “Non-Hermitian ring laser gyroscopes with enhanced Sagnac sensitivity,” *Nature* **576**, 70 (2019).
- [34] Guria, C., Zhong, Q., Ozdemir, S. K., Patil, Y. S., El-Ganainy, R., & Harris, J. G. E., “Resolving the topology of encircling multiple exceptional points,” *Nat. Com-*

- mun., **15**, 1369 (2024).
- [35] Wang, K., Dutt, A., Wojcik, C. C., & Fan, S., “Topological complex-energy braiding of non-Hermitian bands,” *Nature*, **598**, 59-64 (2021).
- [36] Ding, K., Fang, C., & Ma, G., “Non-Hermitian topology and exceptional-point geometries,” *Nat. Rev. Phys.*, **4**, 745-760 (2022).
- [37] J. Doppler, A. A. Mailybaev, J. Böhm, U. Kuhl, A. Girschik, F. Libisch, T. J. Milburn, P. Rabl, N. Moiseyev, and S. Rotter, “Dynamically encircling an exceptional point for asymmetric mode switching,” *Nature* **537**, 76 (2016).
- [38] X. Shu, A. Li, G. Hu, J. Wang, A. Alù, and L. Chen, “Fast encirclement of an exceptional point for highly efficient and compact chiral mode converters,” *Nat. Commun.* **13**, 2123 (2022).
- [39] X.-L. Zhang, T. Jiang, H.-B. Sun, and C. T. Chan, “Dynamically encircling an exceptional point in anti-parity-time symmetric systems: asymmetric mode switching for symmetry-broken states,” *Light Sci. Appl.* **8**, 88 (2019).
- [40] J. B. Khurgin and Y. D. Chong, “Emulating exceptional-point encirclements using imperfect (leaky) photonic components: asymmetric mode-switching and omnipolarizer action,” *Optica* **8**, 563–570 (2021).
- [41] W. Liu, Y. Wu, C.-K. Duan, X. Rong, and J. Du, “Dynamically encircling an exceptional point in a real quantum system,” *Phys. Rev. Lett.* **126**, 170506 (2021)
- [42] O. Svelto and D. C. Hanna, *Principles of Lasers*, Vol. 1, p. 52 (Springer, New York, 2010).
- [43] W. T. Silfvast, *Laser Fundamentals* (Cambridge University Press, 2004).
- [44] J. Beller and L. Shao, “Acousto-optic modulators integrated on-chip,” *Light: Science & Applications*, **11**, 240 (2022).
- [45] Y. Schrödel *et al.*, “Acousto-optic modulation of gigawatt-scale laser pulses in ambient air,” *Nature Photonics*, **18**, 54 (2024).
- [46] M. Liang, A. Minassian, and M. J. Damzen, “High-energy acousto-optic Q-switched alexandrite laser with wavelength tunable fundamental and UV second harmonic generation,” *Optics Express*, **31**, 42428-42438 (2023).
- [47] N. Singh, J. Lorenzen, M. Sinobad, K. Wang, A. C. Lipapis, H. C. Frankis, *et al.*, Silicon photonics-based high-energy passively Q-switched laser, *Nat. Photonics* **18**, 1 (2024).
- [48] M. Wang, S. Huang, Y. J. Zeng, R. Huang, D. Sun, M. Wang, *et al.*, MoO_{3-x} as a wideband optical saturable absorber for passively Q-switching ytterbium-, erbium-, and thulium-doped fiber lasers, *Opt. Mater. Express* **10**, 2480 (2020).
- [49] X. Liu, Z. Hong, Y. Liu, H. Zhang, L. Guo, and X. Ge, “Few-layer TaSe₂ as a saturable absorber for passively Q-switched erbium-doped fiber lasers,” *Opt. Mater. Express*, **11** 385 (2021).
- [50] H. Hodaie, A. U. Hassan, S. Wittek, H. Garcia-Gracia, R. El-ganainy, D. N. Christodoulides, and M. Khajavikhan, “Enhanced sensitivity at higher-order exceptional points,” *Nature* **548**, 187 (2017).
- [51] I. Mandal and E. J. Bergholtz, “Symmetry and Higher-Order Exceptional Points,” *Phys. Rev. Lett.* **127**, 186601 (2021).
- [52] K. Ding, G. Ma, M. Xiao, Z. Q. Zhang, and C. T. Chan, “Emergence, Coalescence, and Topological Properties of Multiple Exceptional Points and Their Experimental Realization,” *Phys. Rev. X* **6**, 021007 (2016).
- [53] S. Dey, A. Laha, and S. Ghosh, “Nonlinearity-induced anomalous mode collapse and nonchiral asymmetric mode switching around multiple exceptional points,” *Phys. Rev. B* **101**, 125432 (2020).
- [54] S.-Y. Lee, J.-W. Ryu, and S. W. Kim, “Analysis of multiple exceptional points related to three interacting eigenmodes in a non-Hermitian Hamiltonian,” *Phys. Rev. A* **85**, 042101 (2012).
- [55] F. Yu, X.-L. Zhang, Z.-N. Tian, Q.-D. Chen, and H.-B. Sun, “General Rules Governing the Dynamical Encircling of an Arbitrary Number of Exceptional Points,” *Phys. Rev. Lett.* **127**, 253901 (2021).
- [56] S.-Y. Lee, J.-W. Ryu, S. W. Kim, and Y. Chung, “Geometric phase around multiple exceptional points,” *Phys. Rev. A* **85**, 064103 (2012).
- [57] R. Nehra and D. Roy, “Topology of multipartite non-Hermitian one-dimensional systems,” *Phys. Rev. B* **105**, 195407 (2022).
- [58] X.-L. Zhang and C. T. Chan, “Dynamically encircling exceptional points in a three-mode waveguide system,” *Commun. Phys.* **2**, 63 (2019).
- [59] A. Hashemi, K. Busch, D. N. Christodoulides, S. K. Ozdemir, and R. El-Ganainy, “Linear response theory of open systems with exceptional points,” *Nat. Commun.* **13**, 3281 (2022).
- [60] S.-Y. Lee, J.-W. Ryu, J.-B. Shim, S.-B. Lee, S. W. Kim, and K. An, “Divergent Petermann factor of interacting resonances in a stadium-shaped microcavity,” *Phys. Rev. A* **78**, 015805 (2008).
- [61] W. Heiss and A. Sannino, “Avoided level crossing and exceptional points,” *J. Phys. A: Math. Gen.* **23**, 1167 (1990).
- [62] H. Eleuch and I. Rotter, “Width bifurcation and dynamical phase transitions in open quantum systems,” *Phys. Rev. E* **87**, 052136 (2013).
- [63] H. Eleuch and I. Rotter, “Open quantum systems and Dicke superradiance,” *Eur. Phys. J. D* **68**, 74 (2014).
- [64] J. Wiersig, “Boundary element method for resonances in dielectric microcavities,” *J. Opt. A: Pure Appl. Opt.* **5**, 53 (2003).
- [65] H.-J. Stöckmann, *Quantum Chaos: An Introduction* (Cambridge University Press, London, 1999).
- [66] F. Haake, *Quantum Signatures of Chaos* (Springer, Berlin, 2010).
- [67] J. von Neumann and E. Wigner, *Phys. Z.* **30**, 467 (1929).
- [68] K.-W. Park, S. Moon, Y. Shin, J. Kim, K. Jeong, and K. An, “Shannon entropy and avoided crossings in closed and open quantum billiards,” *Phys. Rev. E* **97**, 062205 (2018).
- [69] I. Rotter and J. P. Bird, “A review of progress in the physics of open quantum systems: theory and experiment,” *Rep. Prog. Phys.* **78** 114001 (2015).
- [70] B. Zhen, C. W. Hsu, Y. Igarashi, L. Lu, I. Kaminer, A. Pick, S.-L. Chua, J. D. Joannopoulos, and M. Soljačić, “Spawning rings of exceptional points out of Dirac cones,” *Nature* **525**, 354 (2015).
- [71] Szamuel, T. (2009). *Galois groups and fundamental groups* (Vol. 117). Cambridge university press.
- [72] Dummit, David S. and Foote, Richard M. (2004). *Abstract algebra*, Third edition, John Wiley & Sons, Inc., Hoboken, NJ.